Plasma-Catalysis of Non-Oxidative Methane Coupling: A Dynamic Investigation of Plasma and Surface Microkinetics over Ni(111)

Journal:	*The Journal of Physical Chemistry*
Manuscript ID	jp-2022-03503y.R2
Manuscript Type:	Article
Date Submitted by the Author:	n/a
Complete List of Authors:	Maitre, Pierre-andré; University of Aberdeen, School of Engineering Bieniek, Matthew; University of Aberdeen, School of Engineering Kechagiopoulos, Panagiotis; University of Aberdeen, School of Engineering

Plasma-Catalysis of Non-Oxidative Methane Coupling: A Dynamic Investigation of Plasma and Surface Microkinetics over Ni(111)

Pierre-André Maitre, Matthew S. Bieniek, and Panagiotis N. Kechagiopoulos*

Chemical Processes & Materials Group, School of Engineering, University of Aberdeen, Aberdeen, AB24 3UE, UK

E-mail: p.kechagiopoulos@abdn.ac.uk

Abstract

A heterogeneous catalytic microkinetic model is developed and implemented in a zero-dimensional plasma model for the dynamic study of methane non-oxidative coupling over Ni(111) at residence times and power densities consistent with experimental reactors. The microkinetic model is thermodynamically consistent and is parameterised based on the heats of chemisorption of surface species on Ni(111). The surface network explicitly accounts for the interactions of plasma species, namely molecules, radicals and vibrationally excited states with the catalyst active sites via adsorption and Eley-Rideal reactions. The Fridman-Macheret model is used to describe the enhancement of the rate of the dissociative adsorption of vibrationally excited CH_4, H_2 and C_2H_6. In combination with a previously developed detailed kinetic scheme for non-thermal methane plasma, 0D simulation results bring insights on the complex dynamic interactions between the plasma phase and the catalyst during methane non-oxidative coupling. Differential turnover frequencies achieved by plasma-catalysis are higher than those of equivalent plasma-only and catalysis-only simulations combined, however this performance can only be sustained momentarily. Hydrogen produced from dehydrogenation of ethane via electron collisions within the plasma is found to quickly saturate the surface and even promote the conversion of surface CH_3* back to methane.

1 Introduction

Plasma-catalysis is a promising alternative for the direct upgrading of methane into higher-value products, as it allows the conversion of methane at much lower temperatures than traditional thermal-catalytic routes.[1,2] The plasma-activated upgrading of methane in the presence or absence of oxidants has been the subject of numerous experimental investigations in the last two decades. A variety of catalysts and plasma discharges have been studied[3–20] confirming the feasibility of the process. Nonetheless, a commonly reported issue is the lack of understanding of mechanistic details leading to observed performances. Plasma-catalysis systems are highly complex with the plasma affecting the catalyst and vice versa,[21–24] hence modelling has been attracting increasing interest to describe some of the complex interactions.

Recent modelling efforts have focused on the impact of vibrationally excited species to explain the, experimentally observed, synergistic nature of the plasma and catalyst phases. Engelmann et al.[25] studied the non-oxidative coupling of methane on various transition metals using a surface microkinetic model. The work predicted a significant increase in the turnover frequency of vibrationally excited methane for the case of low activity, weakly binding, metals. Loenders et al.[26] used a similar approach to study the partial oxidation of methane on Pt(111) and found that, even though vibrational excitation of methane and oxygen has a positive effect, it is the plasma-generated radicals that govern the surface chemistry. These studies highlighted the need of kinetic models that encompass the range of species that originate from the plasma phase in order to describe their impact on and interactions with the catalyst. Nonetheless, most work to date have investigated only initial rates considering a static gas phase, in which populations of vibrationally excited states were dictated by an a priori decided distribution at a pre-set vibrational temperature. Dynamic studies of plasma-catalysis, where a plasma-kinetic model is solved concurrently to a catalytic surface one have only been reported for the production of ammonia.[27–29] Given that typical discharges used in plasma-catalysis (AC driven or pulsed) are inherently transient

in nature, the dynamic evolution of surface intermediates and gas phase species profiles is of particular interest. Moreover, as recently demonstrated in thermal catalysis by the Dauenhauer group,[30,31] dynamical effects can potentially be exploited to achieve a higher than the steady state performance.

In this respect, the objective of this work is to develop a 0D dynamic model for the non-oxidative coupling of methane that accounts for both plasma and surface kinetics in detail. Temperature is a determining parameter in thermal-catalysis, dictating the activity of the catalyst by influencing its turnover frequency,[32] while within non-thermal plasmas it influences gas-phase radical reactions and relaxation processes of excited species. As the latter lead to an increase of the gas bulk temperature,[2] recent plasma-catalysis modelling studies have considered temperatures higher than ambient.[25,26] To account for this, the impact of temperature on gas and surface processes is investigated in this work in a range from 300 to 600 K at timescales in the order of experimental reactors. Nickel is chosen as a catalyst due to its known capacity to activate $C-H$ bonds and wide application in methane upgrading processes.[5,10,33–37] The Ni(111) facet is considered as it is the most common plane in real polycrystalline supported metal catalysts. The performance of the plasma-catalytic reactor at the different temperatures is further compared with the equivalent plasma-only and catalysis-only reactors to elucidate the interactions of the two phases. For all cases, a reaction pathway analysis is carried out to elaborate on the profiles of gas and surface species obtained and turnover frequency (TOF) values achieved. The energy efficiency of all processes is finally analysed and compared against thermodynamics.

2 Methods

2.1 Reactor design and catalyst characteristics

Simulations are carried out based on the characteristics of a single-sided Dielectric Barrier Discharge (DBD) reactor (Figure 1). In this design, an internal rod of radius $R_g = 11mm$ acts as the ground electrode and is placed concentrically within a quartz tube of internal

radius $R_d = 13mm$ that acts as the reactor's external wall and the dielectric of the DBD. The power electrode is positioned externally to the quartz tube. The plasma is formed within the region between the ground electrode and the dielectric of a length $L = 5mm$ and annular gap $d_{gap} = 2mm$, where the catalyst pellets are also packed. Pure methane is fed at constant flow (see Section 2.2 for the operating conditions considered).

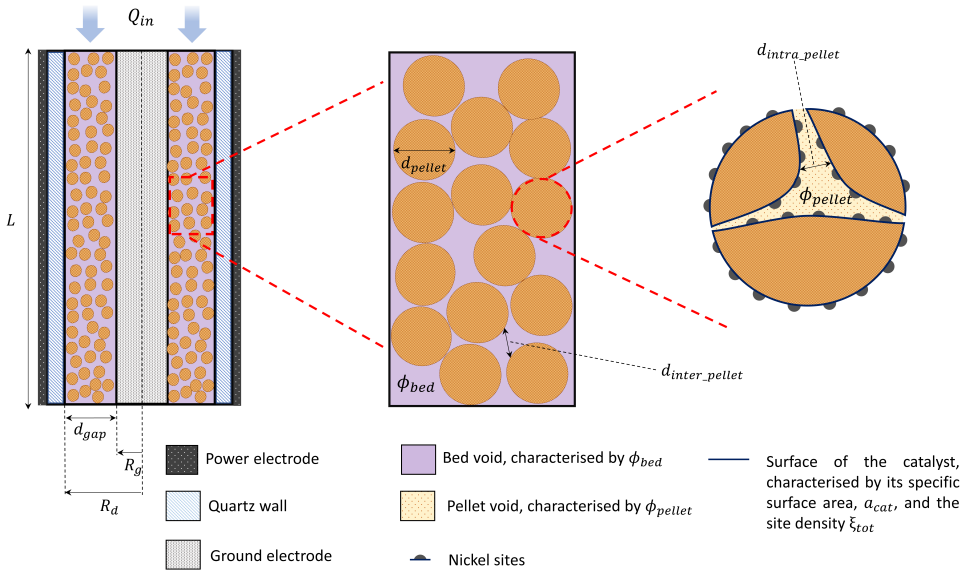

Figure 1: Scheme of the modelled plasma-catalytic reactor, identifying its characteristics across different scales.

The catalyst characteristics are summarised in Table 1). A site density, ξ_{tot}, of 1.8586×10^{19} $sites.m^{-2}$ referring to an fcc Ni(111) lattice plane[38] is used. The specific surface area is of attention, as the value used is 1-2 orders of magnitude lower than typical values of supported catalysts e.g. on silica and titania[33,39] or alumina.[10,20,39] During preliminary simulations, it was seen that the order of magnitude of a_{cat} significantly impacts on the computational cost of the model, relating to the catalyst's surface-to-volume ratio. It was hence decided to use a lower specific surface area value to model efficiently long time scales (see Sections 3.1, 3.2, 3.3, 3.4) and study the impact of higher, more realistic, a_{cat} values on energy efficiency in Section 3.5.

Table 1: Catalyst pellet and bed parameters considered in the simulations.

Parameter	Value
Pellet diameter, $d_{pellet}(mm)$	0.4
Bed porosity, ϕ_{bed} (-)	0.45
Pellet porosity, ϕ_{pellet} (-)	0.5
Pellet density, ρ_{supp} $(kg.m^{-3})$	2300
Surface area, $a_{cat}(m^2.kg^{-1})$	1050
Site density, $\xi_{tot}(sites.m^{-2})$	1.8586×10^{19}

From the geometrical arrangement of the DBD considered and the catalyst parameters presented, catalyst bed characteristics are estimated (see part 1 of Supporting Information (SI)) that are necessary to obtain scaling parameters required to solve the set of continuity equations of the model (see Section 2.3).

2.2 Operating and initial conditions

Different operating conditions are considered to study the nature of the interactions between plasma and catalyst and compare performances with equivalent plasma-only and catalysis-only cases. For all cases, the inlet methane density, n_{β_0}, at different temperatures is the same, resulting in inlet reactor pressures, P_0, that range from 1 bar at 300 K to 2 bar at 600 K (Table 2). A flow, Q_{in}, of pure methane is considered for all cases, with the reactor residence time, τ , obtained from:

$$\tau = \frac{V}{Q_{in}} \tag{1}$$

In the above, V_{reac} and $V_{void-total}$ are used as volume for plasma-only and (plasma)-catalysis cases, respectively (see SI part 1), resulting in larger residence times for the former (Table 2).

For plasma cases, a power, $P_{applied}$, of 50 W, within the range typically applied in DBD reactors[5,13,40,41] is used, resulting in a specific energy input, SEI, of 10 $MJ.m^{-3}$. The very fast dynamics of plasma events coupled with surface reaction dynamics lead to a numerically stiff problem that is challenging and computationally expensive. To facilitate the solution of

the current model, the power density input, P_d, is assumed to be constant (see the energy continuity equation of the electrons in Section 7), and not a sequence of pulse and afterglow periods commonly considered in 0D plasma-only DBD models.[40,42,43] However, as elaborated in Maitre et al.[44] and literature,[40,42,45] methane conversion is mainly driven by the amount of energy inputted per unit of plasma volume (the SEI). It is, therefore, considered that the approach followed allows the qualitative investigation of plasma-catalyst interactions. The power density input, P_d, is thus inferred from the SEI and the residence time of the reactor:

$$P_d = \frac{SEI}{\tau} \tag{2}$$

Simulations are executed for a time equal to 10 τ, with the gas phase containing initially only pure methane and the catalyst surface considered empty. Catalysis-only cases, in addition to the surface reaction network, consider the complete gas phase reaction network from the plasma model, however at zero power input. The trajectories and values obtained at the end of simulations of densities and coverages for all catalysis cases are subject to the initial state of the catalyst surface. Considering that an empty surface is assumed to initialise these simulations, results can be considered as describing the start-up of the reactor or the evolution of the catalyst surface in a pulse-afterglow operation, where the afterglow period is long enough for the surface to alter to a degree it can be considered equivalent to empty.

Table 2: Operating conditions considered. For all cases, initial methane density and flow rate are $\boldsymbol{n_{\beta_0} = 2.45 \times 10^{25} m^{-3}}$ and $\boldsymbol{Q_{in} = 5 \times 10^{-6} m^3.s^{-1}}$.

Case	T_0 (K)	P_0 (bar)	$P_{applied}$ (W)	SEI $(MJ.m^{-3})$	τ (s)	P_d $(W.m^{-3})$
Plasma-only	300	1.00	50	10	0.151	6.6×10^7
	400	1.33				
	500	1.67				
	600	2.00				
Catalysis-only	300	1.00	0	0	0.109	0
	400	1.33				
	500	1.67				
	600	2.00				
Plasma-catalysis	300	1.00	50	10		9.1×10^7
	400	1.33				
	500	1.67				
	600	2.00				

2.3 Continuity equations and scaling parameters

The continuity equations used to model the various reactor types are developed based on certain considerations elaborated in the following, with the rates of the various processes scaled accordingly. For the selected catalyst characteristics and operating conditions, the Debye length is larger than the internal catalyst pore diameter (see SI part 2). Consequently, the plasma and electron collisions are assumed not to occur within the pores of the catalyst pellet.[22] Electronically excited states and ions are also assumed not to be present in the catalyst pores due to their very short lifetimes and low densities.[2,21,46] Radicals and vibrationally excited species have longer lifetimes and higher densities,[2,44,47] hence are considered to be able to enter the catalyst pores and have access to the total catalyst surface area, A_{cat}.

For the charged and the neutral species, denoted with subscripts α and β, respectively, the mass balance equations read:

$$\frac{dn_\alpha}{dt} = \kappa\,\Gamma_{\alpha,e} + \Gamma_{\alpha,g} - L_{\alpha,stick} - \frac{n_\alpha}{\tau} \tag{3}$$

$$\frac{dn_\beta}{dt} = \kappa\,\Gamma_{\beta,e} + \Gamma_{\beta,g} + \Upsilon\,\Gamma_{\beta,c} - L_{\beta,stick} - \frac{n_\beta}{\tau} + \frac{n_{\beta_0}}{\tau} \tag{4}$$

where $\Gamma_e\,(m^{-3}.s^{-1})$, Γ_g $(m^{-3}.s^{-1})$ and $\Gamma_c\,(m^{-2}.s^{-1})$ are the species net formation rates by electron collisions, gas phase reactions (not involving electrons), and catalytic reactions, respectively. $\kappa\,(-)$ is a scaling factor (see Table 3) that accounts for the electron processes not taking place inside the pores of the catalyst. $L_{a/\beta,stick}\,(m^{-3}.s^{-1})$ are the rates of sticking of ions/neutral species, $\frac{n_{\alpha/\beta}}{\tau}$ $(m^{-3}.s^{-1})$ the reactor outlet flow rates and $\frac{n_{\beta_0}}{\tau}$ $(m^{-3}.s^{-1})$ the inlet flow rate (relevant only for the feed methane). The catalytic processes are scaled by a factor Υ (m^{-1}), representing the total surface of the catalyst over the total volume available for gas phase processes (Table 3). This parameter is set to 0 for plasma-only cases.

The sticking rates of ions and neutral species follow the same formalism as in Maitre et al.:[44]

$$L_{\alpha,stick} = \psi_\alpha \sqrt{\frac{k_b T_e}{M_\alpha}} n_\alpha \tag{5}$$

$$L_{\beta,stick} \;=\; s_\beta\,\psi_{\beta s} \sqrt{\frac{3k_b T_0}{M_\beta}} n_\beta \tag{6}$$

where $M\,(kg)$ is the mass of the species considered. The sticking probabilities, $s_\beta(-)$, considered in Maitre et al.[44] are also used in this work, while for ions a value of 1 is assumed. The sticking rates are scaled by a factor ψ (m^{-1}), which corresponds to the ratio of the surface that sticking can occur over the gas volume available to the species, both depending on the reactor case and the species type (see Table 3). For the catalysis cases, it is assumed that the reactor walls and the external surface of the pellets are accessible to ions (see ψ_α in Table 3), while neutral species can only stick on the reactor walls, as catalytic reactions can take place on the catalyst surface (see ψ_β in Table 3).

Table 3: List of scaling parameters and respective values for the different cases simulated.

Scaling parameter	Case	Calculation	Value
$\kappa\,(-)$	Plasma-only	$\kappa = \frac{V_{void-bed}}{V_{void-total}}$	1
	Catalysis		0.62
$\psi_\alpha\,(m^{-1})$	Plasma-only	$\psi_\alpha = \frac{A_{walls}}{V_{reac}}$	1.00×10^3
	Catalysis	$\psi_\alpha = \frac{A_{walls}+A_{ext-bed}}{V_{void-bed}}; A_{ext-bed} = \frac{6}{d_{pellet}} V_{bed}$	1.83×10^4
$\psi_\beta\,(m^{-1})$	Plasma-only	$\psi_\beta = \frac{A_{walls}}{V_{reac}}$	1.00×10^3
	Catalysis	$\psi_\beta = \frac{A_{walls}}{V_{void-total}}$	1.38×10^3
$\Upsilon\,(m^{-1})$	Catalysis	$\Upsilon = \frac{A_{cat}}{V_{void-total}}$	9.18×10^5

Finally, the electron energy continuity equation reads:

$$\frac{dn_\varepsilon}{dt} = P_d - P_{elastic} - P_{inelastic} \tag{7}$$

where $n_\varepsilon = n_e\,\varepsilon$ is the mean electron energy density, P_d the power input density discussed previously, $P_{elastic}$ the power density lost by the electrons in elastic collisions in the gas phase and $P_{inelastic}$ the power density lost in inelastic collisions in the gas phase (namely in excitation, ionisation, and dissociation processes presented in Maitre et al.[44]).

The model is implemented in the Plasimo software,[48] while the Electron Energy Distribution Function (EEDF) is obtained using the BOLSIG+ solver,[49] via the cross-sections used in Maitre et al.[44] The rate constants of all electron collision processes are derived by integration of the collision cross sections over the EEDF following procedures elaborated in the previous work.[44]

2.4 Surface reaction network

The microkinetic model describing the surface reaction network is developed under the assumption that only neutral species can interact with the catalyst active sites. As discussed, given their low densities and short lifetimes, charged species are assumed not to be present in the catalyst pores. Moreover, the energies of ions at plasma-catalysis conditions are typically lower than those required to induce interactions with the surface.[50] Negative surface charging as revealed in recent DFT studies related to CO_2 dissociation can enhance

catalyst activity,[51] hence when similar data become available for CH_4 it would be of value to account for such effects, if present, in global modelling studies. All reactions are considered elementary and reversible, with forward and reverse steps implemented separately. The rate of a given reaction is calculated following the law of mass action. Forward and reverse rate constants are calculated under constraints that ensure thermodynamic consistency (see SI part 3). Adsorption of species can be either molecular (no bond is broken and one site is occupied) or dissociative (two sites required and bond cleavage occurs). Surface reactions follow either the Langmuir-Hinshelwood (two adsorbed species react) or the Eley-Rideal (collision of a gas phase species with a surface one) formalisms. Pre-exponential factors of adsorptions and forward Eley-Rideal reactions are estimated using collision theory. Forward pre-exponential factors of Langmuir-Hinshelwood reactions are obtained using transition state theory estimates. Reverse pre-exponential factors for all reactions are obtained from entropic consistency. Molecular (non-dissociative) adsorptions are considered non-activated. Forward activation barriers for dissociative adsorptions and Langmuir-Hinshelwood reactions are obtained using the unity bond index–quadratic exponential potential (UBI-QEP) method. The method is selected, instead of using directly kinetic data on Ni(111), as it provides a straightforward manner to evaluate the catalytic activity of a range of metals based on a set of well-chosen catalyst descriptors (similar to the use of scaling relationships and/or Brønsted-Evans-Polanyi relationships whose availability, though, for all reactions of interest is not always guaranteed). Forward activation barriers for Eley-Rideal reactions are obtained using the Polanyi-Semenov correlation proposed by Krylov.[52] Reverse activation barriers for all reactions are obtained from enthalpic consistency (see SI part 4).

Based on the low gas phase densities obtained in our previous work,[44] the adsorption of C_3 species is omitted. Methane, ethane and hydrogen are known to adsorb dissociatively,[38] resulting in a total of 10 surface species (CH_3*, CH_2*, $CH*$, $C*$, C_2H_5*, C_2H_4*, C_2H_3*, C_2H_2*, C_2H*, $H*$) being included in the surface model. The microkinetic model is parametrised based on the heats of chemisorption of these species, χ_i, which act as catalyst

descriptors and are taken from the DFT study of Han et al.[38] (see Table 4). For all heat of chemisorption values, the Ni(111) lattice and the most stable position with the lowest binding energy are used. Coverage dependent energetics due to lateral interactions of adsorbates are not considered given the overall low coverages obtained (see Results).

Table 4: Heat of chemisorption values (eV) of considered surface species on Ni(111).[38]

Species	CH_3*	CH_2*	$CH*$	$C*$	C_2H_5*	C_2H_4*	C_2H_3*	C_2H_2*	C_2H*	$H*$
$\boldsymbol{\chi_i}$ **(eV)**	2.02	4.44	6.66	7.03	1.60	0.86	3.07	2.62	5.34	2.68

A total of 58 reversible processes are included in the model, which are presented in detail in the SI (parts 5-7). In brief, ten molecular adsorptions and three dissociative adsorptions, along with their reverse processes, are considered. Once adsorbed, hydrocarbon species can dehydrogenate via seven processes as below:

$$C_xH_y* + * \rightleftharpoons C_xH_{y-1}* + H*$$

or undergo hydrogen transfer via nine processes according to:

$$C_xH_y* + C_zH_w* \rightleftharpoons C_xH_{y-1}* + C_zH_{w+1}*$$

Carbon coupling of species at the surface of the catalyst is possible via two routes:

$$CH_2* + CH_2* \rightleftharpoons C_2H_4*$$

$$CH_3* + CH_2* \rightleftharpoons C_2H_4* + H*$$

Finally, 27 Eley-Rideal processes leading to hydrogen abstraction/addition between surface species and gas phase radicals are included:

$$C_xH_{y+1} + CH_{z-1}* \rightleftharpoons C_xH_y + CH_z*$$

Only adsorbed species containing one carbon atom are considered for Eley-Rideal processes (z=1, 2, 3), whereas the colliding radicals can contain up to three carbon atoms (x=1, 2, 3).

For all vibrationally excited states equivalent surface reactions to those of the respective ground states are considered. Indeed, various studies have demonstrated the strong mode specificity of CH_4 dissociative adsorption on metal surfaces, with vibrational excitation enhancing considerably the adsorption rate in comparison to that of the ground state.[53–55] The contribution of vibrational excitation energy in overcoming the activation barrier of the dissociative adsorption of CH_4, C_2H_6 and H_2 is considered according to the Fridman-Macheret model (see SI part 4). Molecular adsorptions and Eley-Rideal reactions of vibrationally excited states are assumed to proceed with the same rate as that of the ground state. As non-dissociative adsorptions proceed with no barrier, the vibrational energy of excited states is assumed to be dissipated upon adsorption.[50] For Eley-Rideal reactions preliminary simulations revealed the dominant path to be also barrierless, so for simplicity a similar assumption was made. Electronically excited states and ions due to their very low densities and extremely short lifetimes[44] are considered not to interact with the catalyst surface.

Finally, the total balance of active sites is considered:

$$\xi_{tot} = \xi_* + \sum_{i=1}^{n_{species}} \xi_i \tag{8}$$

where ξ_* is the vacant site surface density and ξ_i is the site surface density that is occupied by surface species i.

3 Results and Discussion

3.1 Methane and final products densities

The densities of CH_4 and its excited states, and C_2 products, for all temperatures and reactor cases studied are presented in Figure 2. The results are plotted against normalised

time ($\frac{t}{\tau}$), as the residence time differs between plasma-only and (plasma-) catalysis cases. Figure 2 presents results in logarithmic scale to put focus on the initial highly transient response of the variables, while Figure S1 in the SI (part 8) presents the same results in linear scale to demonstrate the approach to steady state. Density profiles for the main radicals are provided also in the SI (part 9).

Methane and C_2 species densities exhibit similar trends in plasma-only simulations (solid lines in Figure 2), reaching a steady state within a simulation time of approximately 5τ. As the density of CH_4 decreases, that of C_2 species increases, in line with the results presented previously.[44] Temperature variation within the range studied has overall a negligible impact, in agreement with methane thermal decomposition occurring over 800 K.[56] A small increase in the conversion of methane observed with rising temperature is attributed to the acceleration of step $H + CH_4 \rightarrow CH_3 + H_2$, whereas plasma processes remain largely unaffected.

Catalysis-only cases (dashed lines in Figure 2) exhibit a much more transient response, characterised for all temperatures by the density of methane initially decreasing and subsequently increasing. The drop in CH_4 density is due to its adsorption on the surface of the catalyst, which results in a gradual saturation of the catalyst active sites (see Section 3.2). As the surface coverage of CH_x* fragments rises, desorption reactions are promoted resulting in a decrease of the net rate of methane adsorption. Adsorption and desorption reactions of methane eventually equilibrate at approximately 10τ, with methane conversion achieved being very low from that time onwards ($\leqq 1\%$). At 300 K, the adsorption rate of methane is slow, as indicated by the less pronounced decrease in CH_4 density in comparison to the other catalysis-only cases (Figure 2-a). At 400 K, methane adsorption accelerates while its desorption is slower than at 500 and 600 K, resulting in the lowest density of methane achieved. C_2 species densities are at all times very low, given the low conversion of methane. Qualitatively, these results agree with the work from Okolie et al.,[57] who studied non-oxidative coupling of methane over nickel for temperatures lower than 773 K and found

methane conversions below 1.2%.

The plasma-catalysis responses (dashed-dotted lines in Figure 2) initially follow similar trends to those of the catalysis-only cases (Figure 2-a). However, at 400 K, and especially at 500 and 600 K, the lower methane densities achieved evidence a clear effect of plasma interaction with the catalyst. Unlike the equivalent catalysis-only cases where adsorption and desorption of methane balanced over time, during plasma-catalysis simulations the excited states of methane and the radicals originating from the gas phase enhance the conversion of methane (discussed in further detail in Section 3.4). This is confirmed by the densities of C_2 molecules (Figure 2-b), which reach peak values two times higher than the sum of plasma-only and catalysis-only cases. As with the density of methane, a higher production of C_2 is achieved at 500 and 600 K in comparison to 400 K. This confirms the ability of plasma to increase the differential turnover frequency of a catalyst (see Section 3.3) and lead to synergistic effects at temperatures too low for thermal catalysis activity (but above 400 K in our simulations). Nonetheless, as observed also for the catalysis-only cases, the methane density increases again at the later stages of the simulations, due to the increased desorption of CH_4. These trends are a consequence of the high coverage of $H*$ surface species originating from H_2 and H in the plasma phase and are discussed in detail in Section 3.2 elaborating on surface densities and rates.

The populations of $CH_4(\nu 2, 4)$ and $CH_4(\nu 1, 3)$ obtained with plasma-only and plasma-catalysis scenarios are presented in Figures 2-c and 2-d, respectively. Given the absence of plasma, there is no production of excited states in catalysis-only cases. For both plasma cases the densities of $CH_4(\nu 2, 4)$ and $CH_4(\nu 1, 3)$ are on average four and five orders of magnitude lower than those of ground state CH_4 and well below the peak values reported in Maitre et al.[44] and in other studies involving DBDs.[40] These results are due to the discharge being simulated as a homogeneous plasma, with two to three orders of magnitude lower power density inputted than generally applicable in pulse and afterglow models.[40,43,45] Nonetheless, qualitative differences can still be discerned based

on reactor case and temperature. Specifically, lower average densities of excited states are predicted with higher temperature and for plasma-catalysis cases on account of higher rates of Vibrational-Translational (VT) and Vibrational-Vibrational (VV) processes, and faster adsorption rates on the catalyst (these effects being more pronounced for $CH_4(\nu 1,3)$). Interestingly, the density of $CH_4(\nu 2,4)$ during plasma-catalysis and above 300 K follows a similar trend to that of ground state CH_4, passing through a minimum, while the opposite profile is observed for $CH_4(\nu 1,3)$. These trends can be explained by a reduction of the rate of the VV process $CH_4(\nu 1,3) + CH_4 \rightarrow CH_4(\nu 2,4) + CH_4(\nu 2,4)$ due to the consumption of CH_4 on the catalyst, highlighting an effect the catalyst has on plasma species.

Finally, the selectivities of products are not significantly influenced by the temperature and are therefore presented in the SI (part 10). For plasma-only cases, selectivities of 26% for ethane, 50% ethylene and 18% acetylene are obtained for all temperatures (in line with the results of Maitre et al.[44] for a 10 $MJ.m^{-3}$ SEI). For catalytic cases (with or without plasma), the product formation is dominated by the surface chemistry. Ethane accounts for nearly 100% of the products, with only traces of ethylene ($\approx 0.0005\%$) and C_3 species ($\approx 0.0008\%$ propane and $\approx 0.001\%$ propylene), results that compare well with experimental literature of non-oxidative methane coupling over nickel.[36,57]

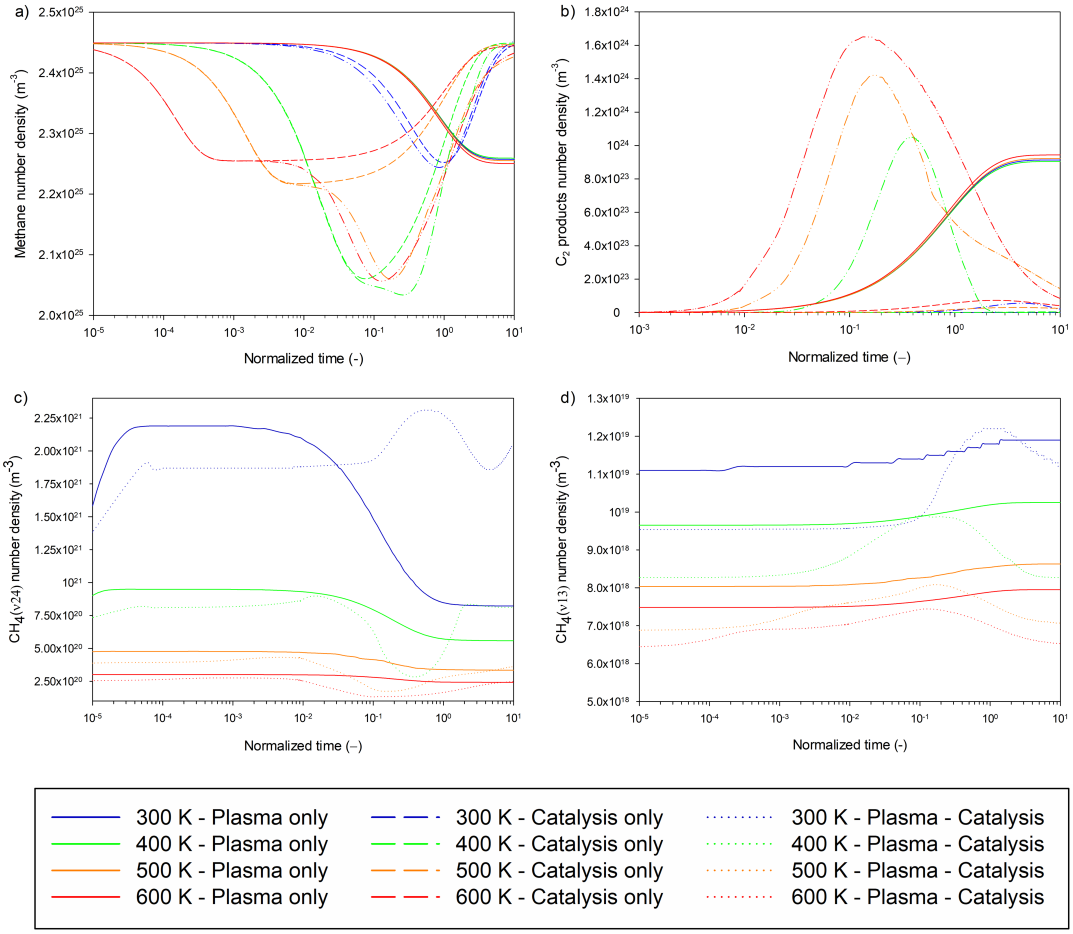

Figure 2: Gas species number densities (m^{-3}) against normalised time in logarithmic scale for the different cases simulated. a) CH_4, b) C_2 species, c) $CH_4(\nu 2, 4)$, d) $CH_4(\nu 1, 3)$. Figure S1 in the SI (part 8) reproduces the same data in linear scale to demonstrate the approach to steady state.

3.2 Surface species and rates

Figure 3 presents the evolution of surface densities of species during catalysis-only (panel a) and plasma-catalysis cases (panel b) at 500 K. This temperature is selected to elaborate on plasma-catalyst interactions, as it is the lowest where significant synergistic effects were observed (Section 3.1). Other temperatures exhibit qualitative similarities (see SI part 11). Partial surface coverages (commonly reported in thermal catalysis microkinetic modelling studies) can be obtained by dividing surface densities values presented below with the active

site density, ξ_{tot}. Figure 4 presents the most important surface (panels a and b) and gas phase (panel c) reaction rates for the plasma-catalysis case at 500 K, with all values scaled per unit volume to facilitate comparison.

Surface densities for catalysis-only and plasma-catalysis cases are initialised at a value $\xi_i = 1 \times 10^5\, m^{-2}$ for all species to approximate an empty catalyst surface (Figure 3). The high density of methane in the gas phase leads to the almost instantaneous rise of CH_3* and $H*$ surface densities to $2 \times 10^{15}\, m^{-2}$ (partial coverage of 0.011%) at the onset of the simulation. For both reactor cases and for approximately 1 ms, the evolution of these primary surface species is identical, rising concurrently up to value of $2.55 \times 10^{18}\, m^{-2}$ (partial coverage of 13%). During this period, the dissociative adsorption of methane is dominant, while its associative desorption gradually rises in rate as the coverage of CH_3* and $H*$ increases (Figure 4-a). The duration of this initial stage, and to a smaller degree the values that the surface densities of CH_3* and $H*$ approach, are affected by temperature. At 300 K, approximately 0.2 s are required for CH_3* and $H*$ to stabilise at $6 \times 10^{18}\, m^{-2}$, whereas at 600 K only 0.1 ms are needed to stabilise at $2 \times 10^{18}\, m^{-2}$ (see SI part 11).

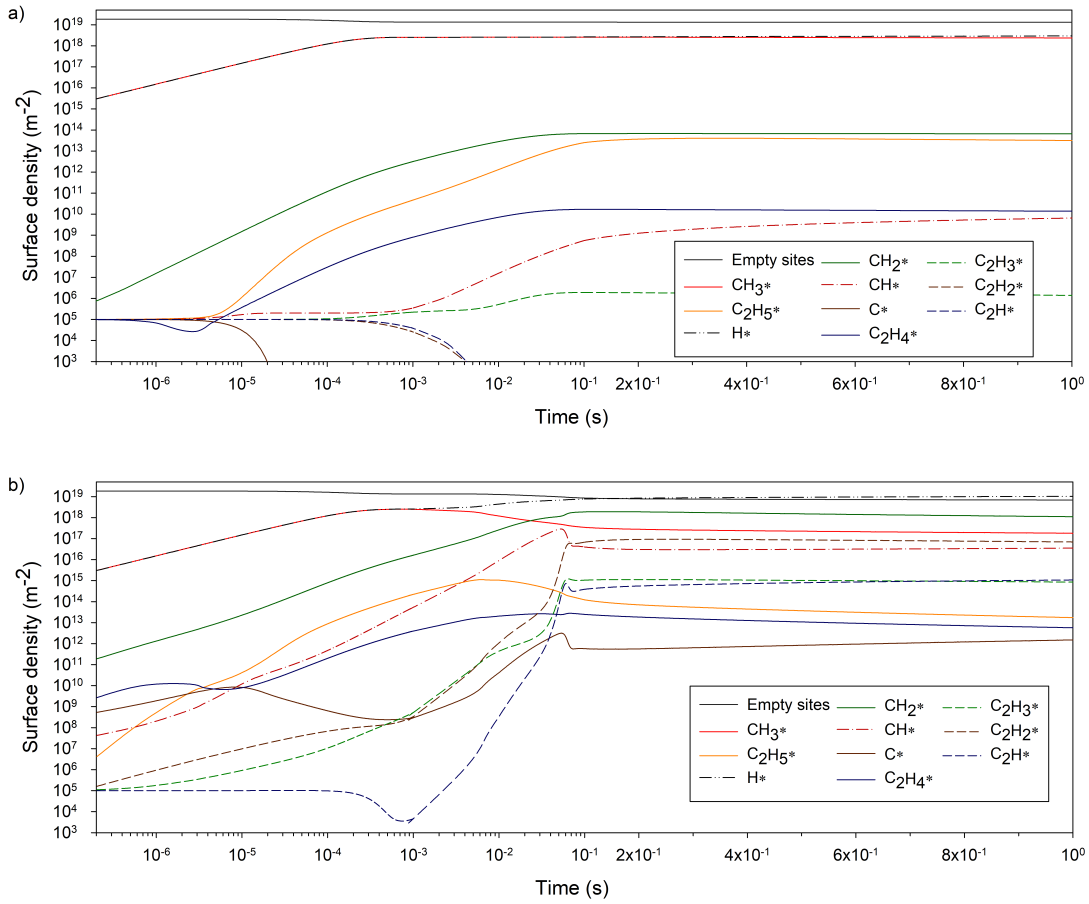

Figure 3: Surface density of adsorbed species (m^{-2}) over time (s) for a) catalysis-only and b) plasma-catalysis cases, at 500 K. For times below 0.1 s the x-axis is logarithmic, and linear afterwards.

In the catalysis-only case the surface is primarily covered by CH_3* and $H*$, the densities of which remain four orders of magnitude higher than the next two most abundant species, CH_2* and C_2H_5* (3-a). CH_2* originates from the dehydrogenation of CH_3*, while C_2H_5* from the coupling of CH_3* and CH_2* species (Section 3.4). C_2H_4* also forms via coupling of CH_x* (more details in Section 3.4.1), while species such as $CH*$ and C_2H_3* appear in later simulation stages due to secondary dehydrogenations of other surface species.

Substantial differences are observed in surface species coverage trends during plasma-catalysis (3-b). After CH_3* and $H*$ have reached a plateau at approximately 1 ms, their surface densities start to diverge, with that of $H*$ increasing further while that of

CH_3* decreasing gradually. The accumulation of $H*$ on the studied timescales, and after 1 ms, is the result of the adsorption/desorption cycle of molecular H_2 being unbalanced (Figure 4-b) on account of complex plasma-catalyst interactions. The rapid dehydrogenation of ethane into ethylene in the gas phase via electron collisions (Figure 4-c) enhances the catalytic production of ethane via the formation of C_2H_4*, see Section 3.4). In turn, this promotes the production of gas phase H_2 and surface $H*$. This cycle explains also the fast and dominant production of ethane versus other C_2 species discussed in the previous section. The progressive saturation of the catalyst surface with $H*$ results in the drastic decrease after 0.018 s of the net adsorption of methane (Figure 4-a), and the catalyst overall having a negative impact on the conversion of methane. This trend is reinforced by Eley-Rideal processes ($CH_3 + CH_x* \rightarrow CH_4 + CH_{x-1}*$) that enhance the production of methane and contribute to the dehydrogenation of surface CH_x* species. Eventually, the surface stabilises to a state where CH_3* production (and methane conversion) is sustained by the dissociative adsorption of $CH_4(\nu 1, 3)$ and $CH_4(\nu 2, 4)$, and the direct adsorption of CH_3 (formed via $CH_4^*(7.9\,eV)$ self-dissociation within the plasma). In parallel, the production of ethane, and consequently its dehydrogenation by electron collisions, and the net adsorption of H_2 (Figure 4-b and -c) decrease.

The formation of C_2H_5* and C_2H_4* follows the formation of CH_3*, with their densities declining concurrently (Section 3.4). C_2H_2* is mostly produced from the adsorption of C_2H_2 at the conditions considered in these simulations. The formation of C_2H* and C_2H_3* ensue from the formation of C_2H_2*. Atomic carbon $C*$, despite its strong binding with Ni(111), maintains very low densities at all stages of the simulation.

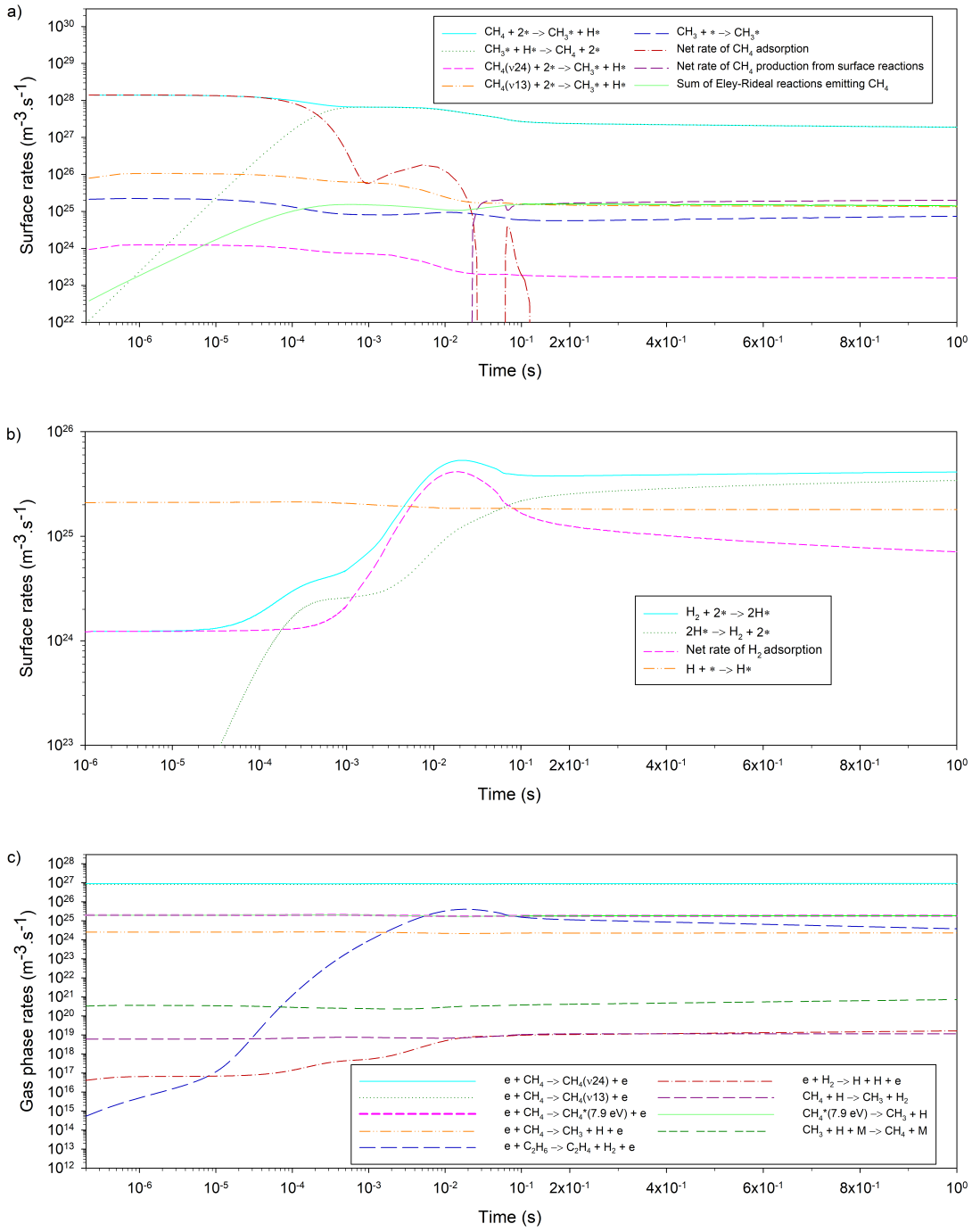

Figure 4: Most significant rates ($m^{-3}.s^{-1}$) over time (s) for plasma-catalysis case at 500 K, a) involving methane at the surface, b) involving hydrogen at the surface, c) in the gas phase. For times below 0.1 s the x-axis is logarithmic, and linear afterwards.

3.3 Turnover frequencies (TOFs)

The catalysis-only and plasma-catalysis cases are further analysed in terms of Turnover Frequency (s^{-1}) of methane (moles consumed) and ethane (moles produced) according to:

$$TOF_{CH_4} = \frac{Q_{in}\,(n_{\beta_0} - n_{CH_4})}{\xi_{tot}\,A_{cat}} \tag{9}$$

$$TOF_{C_2H_6} = \frac{Q_{in}\,n_{C_2H_6}}{\xi_{tot}\,A_{cat}} \tag{10}$$

where $\xi_{tot}\,(sites.m^{-2})$ is the site density and $A_{cat}\,(m^2)$ the total surface of the catalyst. It is assumed that there is no gas expansion in the reactor, so the reactor inlet and outlet volumetric flows are equal.

TOF_{CH_4} profiles naturally mirror those of methane density discussed in Section 3.1. For both reactor cases, the initial increase in TOF_{CH_4} occurs earlier at higher temperatures (Figure 5-a). For catalysis-only, the lower peak value at 300 K indicates the slower adsorption at this temperature, while the higher peak value at 400 K followed by a sharper decrease is due to the faster adsorption and consequent saturation of the catalyst. At 500 and 600 K, TOF_{CH_4} reaches a plateau when the adsorption and desorption of CH_4 equilibrate. The decrease in TOF_{CH_4} visible for all temperatures is due to the negative effects of the catalyst on the conversion of methane discussed previously. As the simulations approach steady-state at approximately 1 s, TOF_{CH_4} at 600 K is higher than at 500 K due to a faster adsorption/desorption cycle. At 300 and 400 K, TOF_{CH_4} profiles continue decreasing, indicative of the eventual catalyst activity loss discussed in Section 3.1.

Plasma-catalysis TOF_{CH_4} profiles follow initially those of catalysis-only. At 300 K, minor differences observed are due to the higher adsorption rates induced by vibrationally excited species and the activation of methane in the gas phase. At higher temperatures, the synergistic effects observed on methane conversion (see Section 3.1) are again visible, with TOF_{CH_4} peak values being larger by a factor of ~2 at 500 and 600 K in comparison to the respective catalysis-only case. A slower decrease at the later stages of the simulations

compared to catalysis-only is also visible, indicative of the beneficial effect of methane activation via plasma processes, despite the still present negative effects of the catalyst presence.

$TOF_{C_2H_6}$ profiles differ over time (Figure 5-b) with temperature again being determining. In the catalysis-only case, values obtained at 500 and 600 K are approximately one and five orders of magnitude higher than those at 400 K and 300 K, respectively. Plasma-catalysis cases demonstrate a significant increase in the peak $TOF_{C_2H_6}$ values compared to the equivalent catalysis-only cases for all temperatures considered, confirming the existence of synergism. The decrease in $TOF_{C_2H_6}$ in later stages of the simulation is more pronounced at 400 K, as a consequence of the unbalanced adsorption/desorption cycles, that saturate the catalyst faster than in other cases.

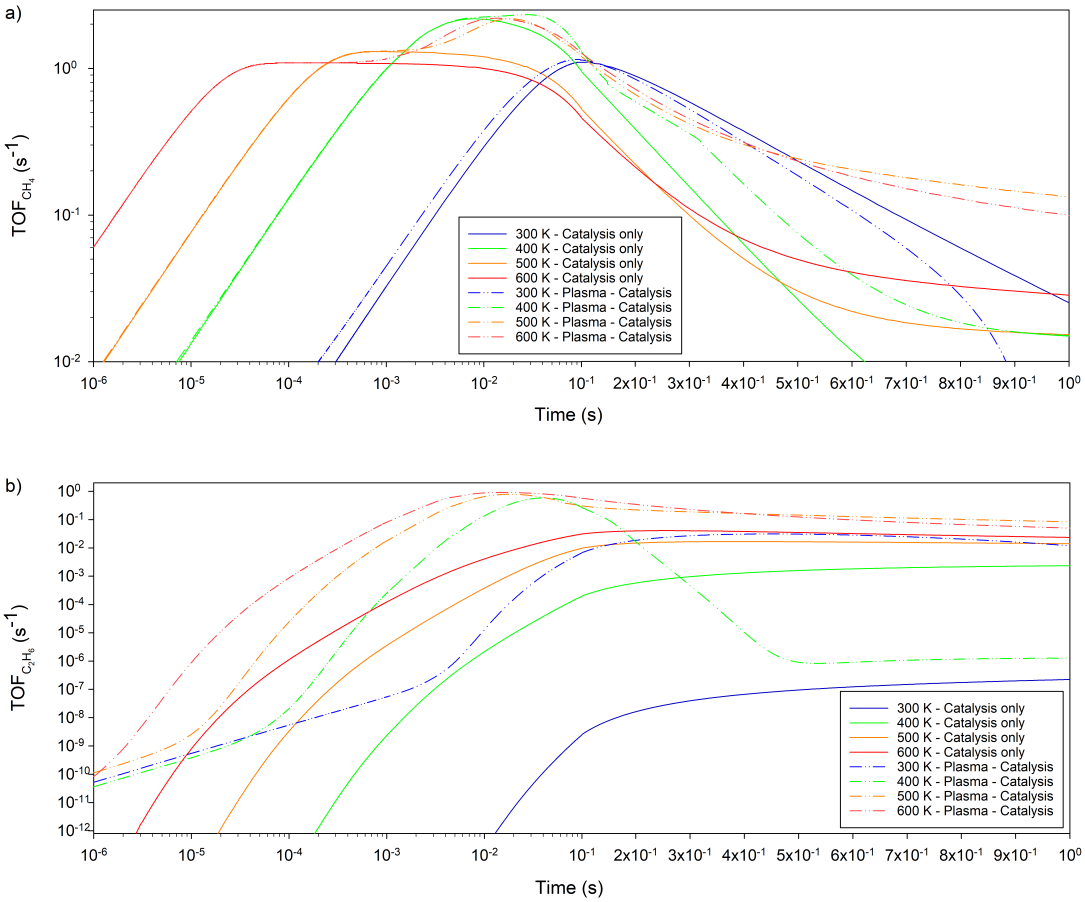

Figure 5: TOF (s^{-1}) over time (s) (for times below 0.1 s the axis is logarithmic, linear afterwards) for the catalytic scenarios and different temperatures studied for a) Methane and b) Ethane.

Table 5 summarises the TOF_{CH_4} values obtained in this work at 500 and 600 K for the two catalysis cases studied. The data obtained at the end of the simulations (for a time of 1 s in Figure 5,) are considered to be steady-state values for these temperatures, while peak values from Figure 5 are also provided for comparison. In Engelmann et al.,[25] one of the very few works that have studied the plasma-catalytic non-oxidative methane via microkinetics, rates at 0% conversion were provided for a variety of transition metals. For Ni(111), at 500 K and a vibrational temperature of 1500 K, initial TOF_{CH_4} values approximately equal to 1 s^{-1} were reported when reactive plasma species were considered, which are in overall good agreement with present peak values. Nonetheless, the current

work resolves further the temporal evolution of TOF_{CH_4}, revealing that the high initial (or peak) rates are not maintained, with the catalyst effectively obstructing plasma driven pathways. In all cases, the proximity of results reported in the two works, within their methodological differences, suggests that UBI-QEP, despite its semi-empirical nature, can be used to estimate surface energetics, particularly in cases where DFT data for obtaining scaling relationships are not readily available. Experimental comparison is more challenging, as methane conversion is typically studied at higher temperatures than those evaluated in the present work. Indicatively, Table 5 presents TOF_{CH_4} values that were reported in methane decomposition experimental works over Ni catalysts. For methane decomposition at 873 K over a Ni/Al_2O_3 catalyst, TOF_{CH_4} values of 0.75 and 0.18 s^{-1} after 0.5 and 3 h of reaction time were reported,[58] while over a Ni/MgO at the same temperature values from almost 4 to 1.69 s^{-1} were measured, the decline in rate observed within only 2 min. Clearly, experimental results are impacted by carbon deposition, an aspect not accounted for in present simulations. Moreover, catalyst structural features like the support material, the metal particle size, and dispersion, further impact experimentally measured rates. This was exemplified in the work of Xu et al.[59] where variation of Ni particle size was seen to be the main controlling parameter for methane decomposition rates. At temperatures closer to those modelled in the current work, Kechagiopoulos et al. reported TOF_{CH_4} values for methane decomposition from 0.1 to 0.32 s^{-1}. In all cases, an order of magnitude agreement with catalysis-only results is observed across a range of experimental works. In combination to the multiple reports successfully having used UBI-QEP[60–63] or Polanyi relationships[64,65] together with chemisorption energies as catalyst descriptors for the microkinetic modelling of high temperature heterogeneously catalysed methane conversion over various metals, an adequate depiction of the purely catalytic reactivity is suggested. Nonetheless, more research is warranted towards a detailed validation of plasma-catalysis microkinetic models.

Table 5: TOF_{CH_4} values obtained via plasma-catalysis microkinetic simulations and experimental results obtained with Ni on various supports for methane decomposition.

Source	Type of work	Temperature	$TOF_{(CH_4)}(s^{-1})$	
Engelmann et al.[25]	Plasma-catalysis microkinetic modelling on Ni(111)	$T_0 = 500\,K$, $T_{vib} = 1500\,K$	≈ 1 (0% conversion)	
Ray et al.[58]	Decomposition over Ni/Al_2O_3	$T_0 = 873\,K$	0.75 (after 0.5 h)	
			0.18 (after 3 h)	
Wei and Iglesia[66]	Decomposition over Ni/MgO	$T_0 = 873\,K$	3.87 (initial)	
			1.69 (after 2 min)	
Xu et al.[59]	Decomposition over Ni on various supports	$T_0 = 923\,K$	0.52 - 2.89 across 9 - 19 nm Ni particle sizes	
Kechagiopoulos et al.[63]	Decomposition over $Ni/La_2O_3 - CeO_2 - ZrO_2$	$T_0 = 673\,K$	≈ 0.1	
		$T_0 = 773\,K$	≈ 0.32	
This work	Catalysis microkinetic modelling on Ni(111)	$T_0 = 500\,K$	1.30 (peak)	0.015 (final)
		$T_0 = 600\,K$	1.09 (peak)	0.028 (final)
	Plasma-catalysis microkinetic modelling on Ni(111)	$T_0 = 500\,K$	2.18 (peak)	0.129 (final)
		$T_0 = 600\,K$	1.15 (peak)	0.949 (final)

3.4 Reaction pathway analysis (RPA)

A reaction pathway analysis is carried out to elucidate the importance of production and consumption pathways in the transformation of species. Rates for the different reactor cases are integrated over a time of $2\,ms$ (t_{integ}) and normalised with their characteristic dimension, namely the total volume available (V_{reac} or V_{void}) for gas rates ($r_{i,g}$) and the total area of the catalyst, A_{cat}, for surface rates ($r_{i,s}$):

$$R_{i,g} = V_{reac/void}\,\frac{\int_{t_{start}}^{t_{start}+t_{integ}} r_{i,g}\,dt}{t_{integ}} \tag{11}$$

$$R_{i,s} = A_{cat} \frac{\int_{t_{start}}^{t_{start}+t_{integ}} r_{i,s}\, dt}{t_{integ}} \quad (12)$$

In the above, R_i are the integrated normalised rates in $particles.s^{-1}$, which provide the number of molecules, radicals, etc. that are produced/consumed during 2 ms.

3.4.1 Carbon transformations

Carbon transformations at 500 K are considered at the time that the net rate of CH_4 consumption is at its peak (Section 3.1), with rates integration (equations 11 and 12) taking place for 2 ms following the peak time. For plasma-only cases, where CH_4 consumption profiles do not peak, integration of rates takes place towards the end of the simulation when steady state has been reached. For comparison, a similar analysis is performed at a later stage of plasma-catalysis simulations when activity has decreased and stabilised.

Figure 6-a presents the reaction pathway analysis for the plasma-only case at simulation time $t_{start} = 1.45\,s$. Results follow those previously elaborated,[44] with the cycle of excitation/de-excitation of vibrationally excited states of methane rates being two orders of magnitude faster than the conversion rates of these states into CH_3. The creation of methyl radicals mostly takes place via the dissociation of the electronically excited state $CH_4^*(7.9\,eV)$. The primary product is ethane, which further dehydrogenates to acetylene via electron collisions. The sticking of CH_3 radicals on the walls of the reactor is limited, accounting for 2.51% of its total consumption.

Catalysis-only reaction pathways at peak simulation time $t_{start} = 0.39\,s$ are much simpler (Figure 6-b). Due to the absence of electron collisions and the temperature of 500 K being too low to thermally activate methane, gas phase activity is negligible. Activation of methane takes place only at the surface of the catalyst via its dissociative adsorption to CH_3* and $H*$. CH_3* is equally consumed by coupling and H-transfer pathways:

$$CH_2* + CH_3* \rightarrow C_2H_4* + H*$$

$$C_2H_4* + CH_3* \rightarrow C_2H_5* + CH_2*$$

Both processes enable the formation of C_2H_5*, which ultimately desorbs associatively as ethane. Eley-Rideal processes have minor contribution to conversion pathways as radicals are scarce at the considered temperature.[56] The most populated radical is CH_3, whole average density of only $1.0 \times 10^7\, m^{-3}$ is orders of magnitude lower that those observed during plasma-only cases ($1.0 \times 10^{20}\, m^{-3}$) and plasma-catalysis ($1.0 \times 10^{18}\, m^{-3}$) ($H$, CH_3 and C_2H_5 density profiles available in SI part 9).

Plasma-catalysis reaction pathways at peak simulation time $t_{start} = 0.018\, s$ share similarities to those of the catalysis-only case, however are significantly more complex (Figure 6-c). Multiple methane activation and excitation mechanisms are present in the plasma phase, enabling also new pathways at the surface of the catalyst. As with the plasma-only case, the cycle of vibrational excitation of methane and its de-excitation via VV and VT processes (integrated rates of $\approx 5 \times 10^{20}\, particles.s^{-1}$) is much faster than any other process (most have integrated rates in the range of $\approx 5 \times 10^{18}\, particles.s^{-1}$). The electronical excitation of methane accounts for the same conversion percentage as in the plasma-only case (2.07%), with $CH_4^*(7.9eV)$ exclusively self-dissociating towards CH_3. Methyl radicals either directly adsorb on the catalyst ($CH_3 + * \rightarrow CH_3*$) at a high conversion contribution of 50.53% or convert back to ground-state methane via the following Eley-Rideal reactions at respective contributions of 56.0%, 39%, 7%, and 3.4%:

$$CH_3 + CH_3* \rightarrow CH_2* + CH_4$$

$$CH_3 + CH_2* \rightarrow CH* + CH_4$$

$$CH_3 + CH* \rightarrow C* + CH_4$$

Adsorption and desorption rates of CH_4 are in the same order of magnitude to that of

VT-VV processes ($\approx 5 \times 10^{20}\, particles.s^{-1}$), however, being quasi-equilibrated (Section 3.2), the net rate of CH_4 adsorption ($5 \times 10^{18}\, particles.s^{-1}$) accounts for only 0.81% of its total consumption. Noteworthy is the enhanced adsorption of $CH_4(\nu 2, 4)$ and $CH_4(\nu 1, 3)$ that provides new channels towards the formation of CH_3*. In line with the results discussed in Section 3.2 and in literature,[25,67] a higher fraction of $CH_4(\nu 1, 3)$ (1.12%) adsorbs on the catalyst in comparison to the other methane states considered (0.81% for CH_4 and 0.028% for $CH_4(\nu 2, 4)$).

CH_3* is the primary species enabling interaction between plasma and catalyst (Section 3.2). 73.63% of CH_3* dehydrogenates to CH_2* according to the Eley-Rideal reactions presented earlier and surface H-transfer ($C_2H_4 * + CH_3* \rightarrow C_2H_5 * + CH_2*$) leading to the shift in surface coverages of these species discussed in Section 3.2 and explaining the net dehydrogenation of CH_3* to CH_2* visible in Figure 6-c. C_2H_5* desorbs as C_2H_6, the latter dehydrogenating in the gas phase via electron collisions ($e + C_2H_6 \rightarrow e + C_2H_4 + H_2$). Ethylene interacts strongly with the catalyst, with nearly 100% of its consumption being due to its adsorption ($C_2H_4 + * \rightarrow C_2H_4*$). 78.10% of the formation of C_2H_4* is due to adsorption, the rest originating from CH_x* coupling:

$$CH_2 * + CH_3* \rightarrow C_2H_4 * + H*$$

The presence of C_2H_4* enables two important surface pathways that are responsible for 79.53% and 20.47% of its consumption, respectively:

$$C_2H_4 * + CH_3* \rightarrow C_2H_5 * + CH_2*$$

$$C_2H_4 * + H* \rightarrow C_2H_5 * + *$$

These processes enhance the production of C_2H_5*, and, consequently, that of ethane in the gas phase versus other C_2 products. The plasma-catalysis process is characterised by

complex dynamic interactions, whereby the production of ethane by the catalyst induces the production of ethylene in the gas phase, which in turn contributes to the consumption of CH_3* towards the formation of C_2H_5* and, ultimately, ethane production in the gas phase.

CH_2* further dehydrogenates to $CH*$ mostly via Eley-Rideal processes $CH_3 + CH_2* \rightarrow CH* + CH_4$ and $CH_2 + CH_2* \rightarrow CH* + CH_3$ at respective contribution of 91.50% and 4.54%, while $C*$ formation is minor due to its effective hydrogenation via process $CH_3* + C* \rightarrow CH_2* + CH*$. Finally, acetylene produced in the gas-phase mostly adsorbs on the catalyst. C_2H_2* is the only source of C_2H* and C_2H_3*, the latter species converting solely to C_2H_4* (pathways omitted in Figure 6-c due to their low rate of $5 \times 10^{13}\, particles.s^{-1}$).

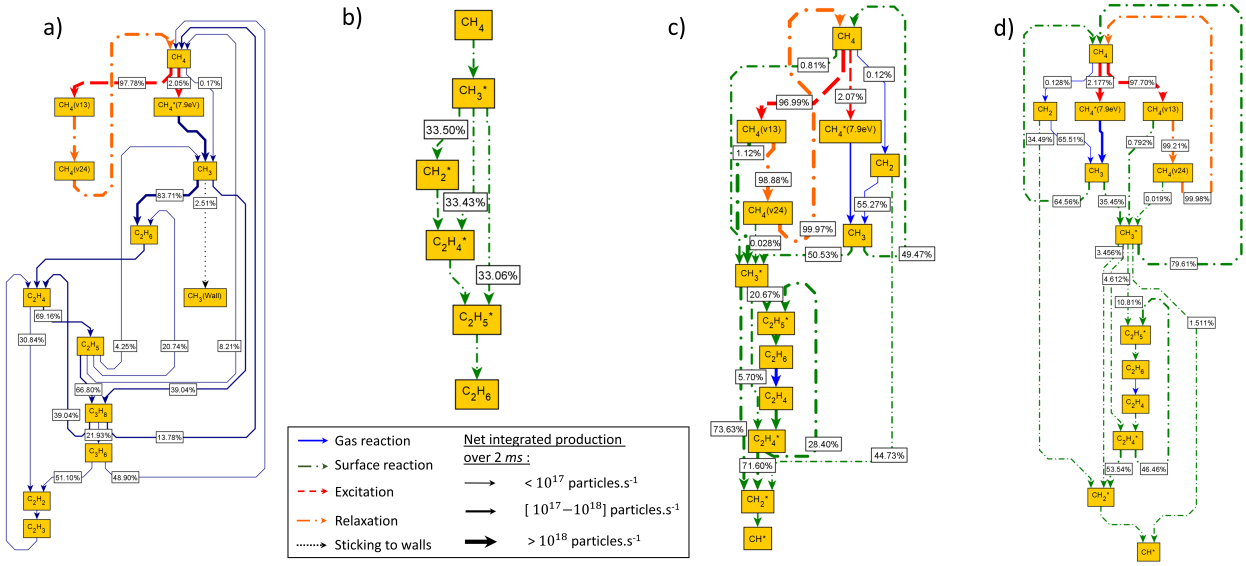

Figure 6: Reaction pathway analysis of carbon at 500 K and at maximum CH_4 consumption for a) plasma-only, b) catalysis-only, c) plasma-catalysis cases, and for stabilised performance for d) plasma-catalysis case.

A similar analysis is performed at a later stage of the plasma-catalysis simulation (simulation time $t_{start} = 1.05\, s$), when the catalyst was observed to have a detrimental effect on the conversion of methane (Section 3.1). The results presented in Figure 6-d resemble the pathways discussed for the peak performance (Figure 6-c), exhibiting however two notable differences. Most importantly, the net production between CH_4 and CH_3* is in the direction towards methane, indicative of its desorption at this stage being faster than its adsorption.

Additionally, the net rate between C_2H_6 and C_2H_4 in the gas phase is approximately ten times lower than that at peak performance, as at this stage of the simulation the hydrogen produced from ethane's dehydrogenation is responsible for the overall lower activity.

3.4.2 Effect of temperature on the reaction pathways of CH_3* and $H*$

A contribution analysis is further performed for the plasma-catalysis case with focus on CH_3* and $H*$ species to investigate the impact of gas temperature. As in the previous section, normalised rates are integrated for 2 ms starting at the peak time in CH_4 consumption. Net rates are calculated for reversible processes and are written in the dominant direction. Results are presented in Figure 7, while in the SI (part 12) a similar analysis is provided for C_2H_5* and C_2H_4*, species whose pathways that showed much less variation across temperature.

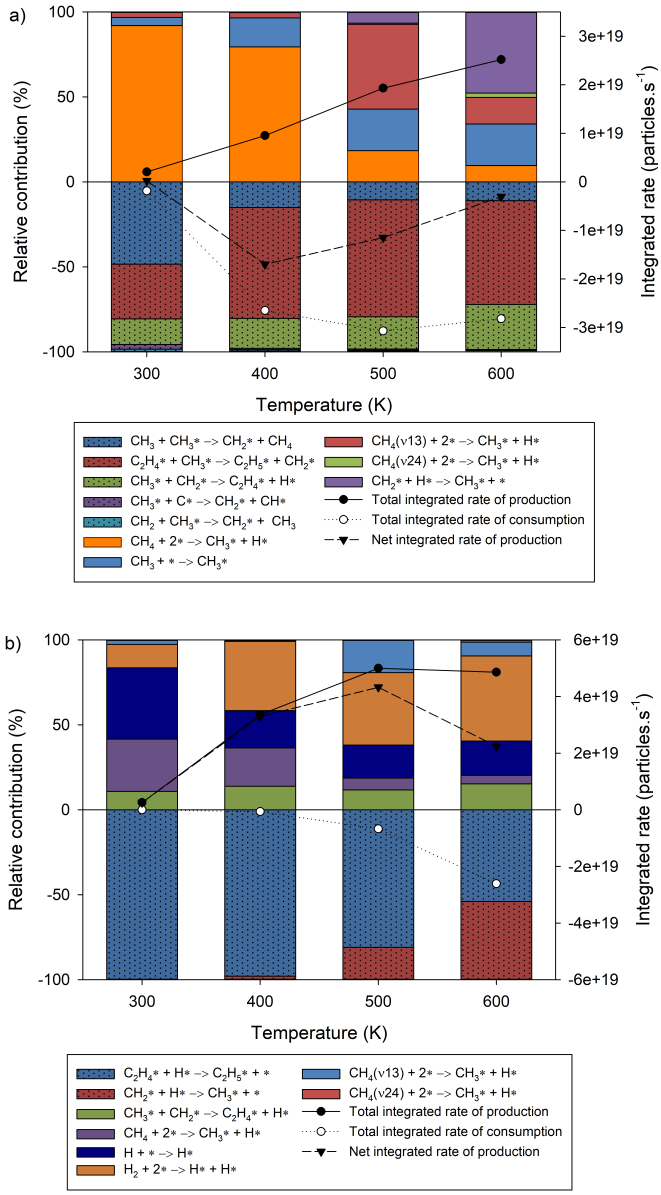

Figure 7: Reaction pathway analysis of a) CH_3* and b) $H*$. Relative contribution (%) and total integrated rates ($particles.s^{-1}$) over temperature (K).

At 300 K, CH_3* accumulates on the catalyst (confirmed by its integrated net rate of formation being marginally positive). Conversely, at all other temperatures CH_3* acts as a reactant, as indicated by its negative net rate of formation (Figure 7-a). Consumption of CH_3* is most pronounced at 400 K due to slow desorption of methane, while at 500 and 600 K the main CH_3* consumption processes involve surface coupling and hydrogen

transfers towards C_2H_5* and C_2H_4* formation. The relative contribution of Eley-Rideal process $CH_3 + CH_3* \rightarrow CH_2 * + CH_4$ decreases with temperature. The contribution of the dissociative adsorption of ground state methane in the production of CH_3* decreases drastically above 400 K as the reverse process accelerates at 500 and 600 K. At 400 K and higher, the dissociative adsorption of vibrationally excited states of methane is dominant. With net rates of 6.45×10^{16}, 2.99×10^{16}, 9.60×10^{18} and 3.93×10^{18} $particles.s^{-1}$ at 300, 400, 500 and 600 K, respectively, the dissociative adsorption of $CH_4(\nu 1, 3)$ is seen to maximise at 500 K. At this temperature, a balance between catalyst activity and excited species populations is achieved, with $CH_4(\nu 1, 3)$ adsorption rates higher than at 300 and 400 K, but rates of VV processes lower than at 600 K (Section 3.1). These positive effects manage to counterbalance the lower density of $CH_4(\nu 1, 3)$, which overall has a higher importance in CH_3* production than $CH_4(\nu 2, 4)$ for all considered temperatures. These findings are primarily an outcome of the higher internal energy of the $CH_4(\nu 1, 3)$ state versus that of $CH_4(\nu 2, 4)$, however, qualitatively, compare well with the works of Juurlink et al.[67] and Chen et al.[68] on Ni(111), who found the stretching modes to be much more efficient in promoting methane's adsorption than the bending modes.

The accumulation of $H*$, discussed throughout this work, is confirmed by its positive integrated net rate of formation (Figure 7-b). At 300 and 400 K the consumption of $H*$ is effectively zero. The production of $H*$ via the adsorption of the H radical is pronounced at 300 K, whereas at higher temperatures the dissociative adsorption of H_2 increases in importance as an outcome of the dehydrogenation of ethane in the gas phase that enhances also the H_2 density. Reaction pathway analysis results for hydrogen presented in the SI (part 13) indicate that the dissociative adsorption of H_2 is even faster than its vibrational excitation. Finally, similar trends to those observed for CH_3* production by the adsorption of $CH_4(\nu 1, 3)$ and CH_4 are visible also for the formation of $H*$, although to a less pronounced effect.

3.5 Energy efficiency

The energy efficiency $E_{eff}\,(T_0)$ for the plasma-catalysis and plasma-only cases is compared at the different temperatures studied. The energy efficiency is defined as the ratio of the reaction enthalpy of the overall transformation of methane to the energy cost of the plasma:

$$E_{eff}\,(T_0) = \frac{(n_{\beta_0} - n_{CH_4})\,\Delta H_r(T_0)}{\tau\,P_d\,N_A} \tag{13}$$

with N_A being the Avogadro number. For the estimation of $\Delta H_r(T_0)$ the selectivities of products, $S_{C_xH_y,i}$, and their corresponding reaction enthalpies from methane at the respective temperature, $\Delta H_{r,i}(T_0)$, are considered (see SI part 14 for details):

$$\Delta H_r(T_0) = \sum_{i}^{n_{products}} S_{C_xH_y,i}\,\Delta H_{r,i}(T_0) \tag{14}$$

As with the reaction pathway analysis, the energy efficiency is calculated at the peak performance time of the simulations. Moreover, the impact of the specific surface area of the catalyst, a_{cat}, is investigated by studying values up to 25 times higher than the base case (a_{cat}= 1050 $m^2.g^{-1}$). Due to the very low activity observed at 300 K, this temperature is omitted from the analysis. Results are finally compared also to a theoretical maximum, which corresponds to the energy efficiency obtained for complete conversion of methane to ethane at the power density of plasma-catalytic runs, namely when $n_{CH_4} = 0\,m^{-3}$, $S_{C_2H_6} = 1\,(-)$, and $P_d = 9.1 \times 10^7\,W.m^{-3}$ (see also Section 2.2).

The theoretical maximum energy efficiency is found to be approximately 14%, with minor variation amongst the different temperatures studied. This corresponds to an optimal energy cost in this DBD reactor of 5.79 $MJ.mol^{-1}_{CH_4}$, which compares well with values reported by SriBala et al.[69] in a glow electrical discharge ranging from 5 to 5.5 $MJ.mol^{-1}_{CH_4}$. These values are directly derived from methane conversion, which mainly depends on the molar flow of methane and the power density in the reactor.[42] The low energy efficiency even at the optimal case is a frequently reported issue with atmospheric pressure DBD reactors, which are subject

to substantial energy losses due to the relaxation of excited species. Atmospheric pressure thermal discharges such as gliding arcs or sparks achieve efficiencies from 40% to 50% as they benefit from both thermal and plasma activation of methane. Microwave plasmas operating at low pressure reach efficiency values of approximately 20%,[41] also higher than DBD.

The energy efficiency for the plasma-only case is approximately 3% (Figure 8), consistent with various works having reported values below 10%.[18,41,43,70] As mentioned, this poor energy efficiency is mainly due to a high proportion of the energy consumed in the vibrational excitation of methane being lost through relaxation processes.[44,71]

The base plasma-catalysis case (a_{cat}= 1050 $m^2.g^{-1}$) has an even lower efficiency compared to the plasma-only case at about 2% on account of two effects. Firstly, $\Delta H_r(T_0)$ is about 50% lower for plasma-catalysis, as the selectivity towards ethane is 100%, while in plasma-only cases all C_2 species have approximately the same selectivity. Secondly, in plasma-catalysis the power density is higher compared to plasma-only. However, as can be seen in Figure 8, the energy efficiency increases substantially at higher specific surface areas, reaching close to the theoretical maximum for a value of 21000 $m^2.g^{-1}$. These results agree well with the work of Kasinathan et al.,[72] whose energy efficiency was estimated to be 10.8%,[41] and the work of Taheraslani and Gardeniers,[18] who reported energy efficiencies from 8 to 11% in the presence of a γ-alumina supported Pd catalyst.

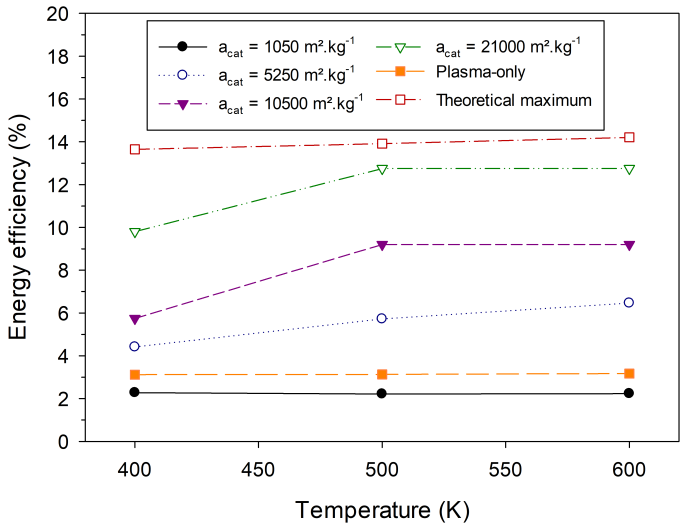

Figure 8: Energy efficiency (%) over gas temperature (K) for the plasma-only case and various specific surface area of the catalyst, a_{cat}, in the plasma-catalysis case.

4 Conclusions

The non-oxidative coupling of methane over Ni(111) was studied via a dynamic 0D plasma-catalytic model, comprising of detailed plasma and surface reaction networks, explicitly describing the interactions of plasma and surface species. A gas bulk temperature from 300 to 600 K was considered with equivalent plasma-only and catalysis-only cases also simulated, in order to discern the plasma and catalyst contributions. Results showed that significant synergistic effects could only be observed at 500 K and above, where a fast turnover of species on the catalyst was achieved. In good agreement with experimental literature, Ni(111) was found to be selective almost exclusively towards ethane, with only traces of ethylene being also produced. However, molecular hydrogen originating from the dehydrogenation of ethane in the plasma was seen to progressively saturate the catalyst surface, which reduced the performance of the plasma-catalysis system by promoting hydrogenation of CH_3* back to methane.

The model further allowed to observe the effect of reactive species from the plasma, such as vibrationally excited methane and radicals, on the surface species and reactions. The

most notable contribution was that of $CH_4(\nu 1, 3)$ at $500\,K$, a temperature where the species was found to be efficiently adsorbing of the catalyst, with VV processes not consuming it excessively in the plasma. The direct adsorption of CH_3 from the gas phase was significant, however the same radical was also observed to accelerate the formation of CH_4 via Eley-Rideal reactions on CH_x* surface species.

Finally, the energy efficiency of the process was found to be highly sensitive to the area to volume ratio of the catalyst. Plasma-catalysis does not necessarily lead to better efficiency compared to plasma alone, stressing the need for operating conditions optimisation. The model presented in this work can be employed to design experiments, while using the heats of chemisorption of surface species as catalyst descriptors allows the investigation of other metals in a straightforward manner.

Supporting Information Available

Catalytic bed characteristics; Kinetic model parameters calculation; List of reactions in the model; Density profiles of main radicals; Product selectivities and methane conversion tables; Surface densities profiles for all temperatures; Reaction pathway analyses for C_2H_4*, C_2H_5* and H_2; Reaction enthalpies considered in the energy efficiency calculations (PDF)

Acknowledgement

We acknowledge and greatly appreciate the assistance from Dr. Mihailova from Plasma Matters B.V. in working with the software Plasimo and from Dr Marcus Campbell Bannerman from the University of Aberdeen for providing access to the computational cluster used for carrying out the simulations in this work.

The work was supported by the UK Engineering and Physical Sciences Research Council (EPSRC) New Investigator Award, grant no. EP/R031800/1.

Author Accepted Manuscript version arising.

References

(1) Puliyalil, H.; Lašič Jurković, D.; Dasireddy, V. D. B. C.; Likozar, B. A review of plasma-assisted catalytic conversion of gaseous carbon dioxide and methane into value-added platform chemicals and fuels. *RSC Advances* **2018**, *8*, 27481–27508.

(2) Nozaki, T.; Okazaki, K. Non-thermal plasma catalysis of methane: Principles, energy efficiency, and applications. *Catalysis Today* **2013**, *211*, 29–38.

(3) Nozaki, T.; Tsukijihara, H.; Fukui, W.; Okazaki, K. Kinetic Analysis of the Catalyst and Non-thermal Plasma Hybrid Reaction for methane Steam Reforming. *Energy Fuels* **2007**, *21*, 2525–2530.

(4) Julian, I.; Ramirez, H.; Hueso, J. L.; Mallada, R.; Santamaria, J. Non-oxidative methane conversion in microwave-assisted structured reactors. *Chemical Engineering Journal* **2019**, *377*, 119764.

(5) Lašič Jurković, D.; Liu, J.-L.; Pohar, A.; Likozar, B. Methane Dry Reforming over Ni/Al_2O_3 Catalyst in Spark Plasma Reactor: Linking Computational Fluid Dynamics (CFD) with Reaction Kinetic Modelling. *Catalysis Today* **2021**, *362*, 11–21.

(6) Sheng, Z.; Kim, H.-H.; Yao, S.; Nozaki, T. Plasma-chemical promotion of catalysis for CH_4 dry reforming: unveiling plasma-enabled reaction mechanisms. *Physical Chemistry Chemical Physics* **2020**, *22*, 19349–19358.

(7) Khoja, A. H.; Tahir, M.; Saidina Amin, N. A. Process optimization of DBD plasma dry reforming of methane over $Ni/La_2O_3MgAl_2O_4$ using multiple response surface methodology. *International Journal of Hydrogen Energy* **2019**, *44*, 11774–11787.

(8) Kim, J.; Go, D. B.; Hicks, J. C. Synergistic effects of plasma–catalyst interactions for CH_4 activation. *Physical Chemistry Chemical Physics* **2017**, *19*, 13010–13021.

(9) Bae, J.; Lee, M.; Park, S.; Jeong, M.-G.; Hong, D.-Y.; Kim, Y. D.; Park, Y.-K.; Hwang, Y. K. Investigation of intermediates in non-oxidative coupling of methane by non-thermal RF plasma. *Catalysis Today* **2017**, *293-294*, 105–112.

(10) de Araújo Moreira, T. G.; de Carvalho Filho, J. F. S.; Carvalho, Y.; de Almeida, J. M. A. R.; Nothaft Romano, P.; Falabella Sousa-Aguiar, E. Highly stable low noble metal content rhodium-based catalyst for the dry reforming of methane. *Fuel* **2021**, *287*, 119536.

(11) Górska, A.; Krawczyk, K.; Jodzis, S.; Schmidt-Szałowski, K. Non-oxidative methane coupling using $Cu/ZnO/Al_2O_3$ catalyst in DBD. *Fuel* **2011**, *90*, 1946–1952.

(12) Chiremba, E.; Zhang, K.; Kazak, C.; Akay, G. Direct nonoxidative conversion of methane to hydrogen and higher hydrocarbons by dielectric barrier discharge plasma with plasma catalysis promoters. *AIChE Journal* **2017**, *63*, 4418–4429.

(13) Delikonstantis, E.; Scapinello, M.; Stefanidis, G. D. Low energy cost conversion of methane to ethylene in a hybrid plasma-catalytic reactor system. *Fuel Processing Technology* **2018**, *176*, 33–42.

(14) Lee, H.; Lee, D.-H.; Song, Y.-H.; Choi, W. C.; Park, Y.-K.; Kim, D. H. Synergistic effect of non-thermal plasma–catalysis hybrid system on methane complete oxidation over Pd-based catalysts. *Chemical Engineering Journal* **2015**, *259*, 761–770.

(15) Michielsen, I.; Uytdenhouwen, Y.; Bogaerts, A.; Meynen, V. Altering Conversion and Product Selectivity of Dry Reforming of Methane in a Dielectric Barrier Discharge by Changing the Dielectric Packing Material. *Catalysts* **2019**, *9*, 51.

(16) García-Moncada, N.; Cents, T.; van Rooij, G.; Lefferts, L. Minimizing carbon deposition in plasma-induced methane coupling with structured hydrogenation catalysts. *Journal of Energy Chemistry* **2020**,

(17) Ranganathan, R. V.; Jony, B.; Fondriest, S. M.; Liu, Z.; Wang, R.; Uddi, M. Plasma-catalysis chemical looping CH_4 reforming with water splitting using ceria supported Ni based La-perovskite nano-catalyst. *Journal of CO_2 Utilization* **2019**, *32*, 11–20.

(18) Taheraslani, M.; Gardeniers, H. Plasma Catalytic Conversion of CH_4 to Alkanes, Olefins and H_2 in a Packed Bed DBD Reactor. *Processes* **2020**, *8*, 774.

(19) Andersen, J. A.; Christensen, J. M.; Østberg, M.; Bogaerts, A.; Jensen, A. D. Plasma-catalytic dry reforming of methane: Screening of catalytic materials in a coaxial packed-bed DBD reactor. *Chemical Engineering Journal* **2020**, *397*, 125519.

(20) Chawdhury, P.; Wang, Y.; Ray, D.; Mathieu, S.; Wang, N.; Harding, J.; Bin, F.; Tu, X.; Subrahmanyam, C. A promising plasma-catalytic approach towards single-step methane conversion to oxygenates at room temperature. *Applied Catalysis B: Environmental* **2021**, *284*, 119735.

(21) Maitre, P.-A.; Bieniek, M. S.; Kechagiopoulos, P. Plasma-enhanced catalysis for the upgrading of methane: A review of modelling and simulation methods. *Reaction Chemistry & Engineering* **2020**, 814–837.

(22) Bogaerts, A.; Zhang, Q.-Z.; Zhang, Y.-R.; Van Laer, K.; Wang, W. Burning questions of plasma catalysis: Answers by modeling. *Catalysis Today* **2019**, *337*, 3–14.

(23) Chen, H.; Mu, Y.; Xu, S.; Xu, S.; Hardacre, C.; Fan, X. Recent advances in non-thermal plasma (NTP) catalysis towards C1 chemistry. *Chinese Journal of Chemical Engineering* **2020**, *28*, 2010–2021.

(24) Neyts, E. C.; Bogaerts, A. Understanding plasma catalysis through modelling and simulation—a review. *Journal of Physics D: Applied Physics* **2014**, *47*, 224010.

(25) Engelmann, Y.; Mehta, P.; Neyts, E. C.; Schneider, W. F.; Bogaerts, A. Predicted Influence of Plasma Activation on Nonoxidative Coupling of Methane on Transition Metal Catalysts. *ACS Sustainable Chemistry & Engineering* **2020**, *8*, 6043–6054.

(26) Loenders, B.; Engelmann, Y.; Bogaerts, A. Plasma-Catalytic Partial Oxidation of Methane on Pt(111): A Microkinetic Study on the Role of Different Plasma Species. *Journal of Physical Chemistry C* **2021**,

(27) Veer, K. v. t.; Reniers, F.; Bogaerts, A. Zero-dimensional modeling of unpacked and packed bed dielectric barrier discharges: the role of vibrational kinetics in ammonia synthesis. *Plasma Sources Science and Technology* **2020**, *29*, 045020.

(28) Veer, K. v. t.; Alphen, S. V.; Remy, A.; Gorbanev, Y.; Geyter, N. D.; Snyders, R.; Reniers, F.; Bogaerts, A. Spatially and temporally non-uniform plasmas: microdischarges from the perspective of molecules in a packed bed plasma reactor. *Journal of Physics D: Applied Physics* **2021**,

(29) Hong, J.; Pancheshnyi, S.; Tam, E.; Lowke, J. J.; Prawer, S.; Murphy, A. B. Kinetic modelling of NH_3 production in N_2–H_2 non-equilibrium atmospheric-pressure plasma catalysis. *Journal of Physics D: Applied Physics* **2017**, *50*, 154005.

(30) Ardagh, M. A.; Birol, T.; Zhang, Q.; Abdelrahman, O. A.; Dauenhauer, P. J. Catalytic resonance theory: superVolcanoes, catalytic molecular pumps, and oscillatory steady state. *Catal. Sci. Technol.* **2019**, *9*, 5058–5076.

(31) Ardagh, M. A.; Abdelrahman, O. A.; Dauenhauer, P. J. Principles of Dynamic Heterogeneous Catalysis: Surface Resonance and Turnover Frequency Response. *ACS Catalysis* **2019**, *9*, 6929–6937.

(32) Whitehead, J. C. Plasma–catalysis: the known knowns, the known unknowns and the unknown unknowns. *Journal of Physics D: Applied Physics* **2016**, *49*, 243001.

(33) Pizzolitto, C.; Pupulin, E.; Menegazzo, F.; Ghedini, E.; Di Michele, A.; Mattarelli, M.; Cruciani, G.; Signoretto, M. Nickel based catalysts for methane dry reforming: Effect of supports on catalytic activity and stability. *International Journal of Hydrogen Energy* **2019**, *44*, 28065–28076.

(34) de Dios García, I.; Stankiewicz, A.; Nigar, H. Syngas production via microwave-assisted dry reforming of methane. *Catalysis Today* **2021**, *362*, 72–80.

(35) Kim, J.; Abbott, M. S.; Go, D. B.; Hicks, J. C. Enhancing C–H Bond Activation of Methane via Temperature-Controlled, Catalyst–Plasma Interactions. *ACS Energy Letters* **2016**, *1*, 94–99.

(36) Nozaki, T.; Muto, N.; Kado, S.; Okazaki, K. Dissociation of vibrationally excited methane on Ni catalyst. *Catalysis Today* **2004**, *89*, 57–65.

(37) Nozaki, T.; Muto, N.; Kadio, S.; Okazaki, K. Dissociation of vibrationally excited methane on Ni catalyst. *Catalysis Today* **2004**, *89*, 67–74.

(38) Han, Z.; Yang, Z.; Han, M. Comprehensive investigation of methane conversion over Ni(111) surface under a consistent DFT framework: Implications for anti-coking of SOFC anodes. *Applied Surface Science* **2019**, *480*, 243–255.

(39) Hasnan, N. S. N.; Timmiati, S. N.; Lim, K. L.; Yaakob, Z.; Kamaruddin, N. H. N.; Teh, L. P. Recent developments in methane decomposition over heterogeneous catalysts: an overview. *Mater Renew Sustain Energy* **2020**, *9*, 8.

(40) Heijkers, S.; Aghaei, M.; Bogaerts, A. Plasma-Based CH_4 Conversion into Higher Hydrocarbons and H_2 : Modeling to Reveal the Reaction Mechanisms of Different Plasma Sources. *Journal of Physical Chemistry C* **2020**, *124*, 7016–7030.

(41) Scapinello, M.; Delikonstantis, E.; Stefanidis, G. D. The panorama of plasma-assisted non-oxidative methane reforming. *Chemical Engineering and Processing: Process Intensification* **2017**, *117*, 120–140.

(42) Toth, J. R.; Shen, X.; Lacks, D. J.; Sankaran, R. M. Reaction Conversion for a Plasma-Based Steady-State Flow Process Is Independent of Reactor Volume. *Industrial & Engineering Chemistry Research* **2018**, *57*, 6048–6056.

(43) Snoeckx, R.; Aerts, R.; Tu, X.; Bogaerts, A. Plasma-Based Dry Reforming: A Computational Study Ranging from the Nanoseconds to Seconds Time Scale. *The Journal of Physical Chemistry C* **2013**, *117*, 4957–4970.

(44) Maitre, P. A.; Bieniek, M. S.; Kechagiopoulos, P. N. Modelling excited species and their role on kinetic pathways in the non-oxidative coupling of methane by dielectric barrier discharge. *Chemical Engineering Science* **2021**, *234*, 116399.

(45) Chen, X.; Zhang, S.; Li, S.; Zhang, C.; Pan, J.; Murphy, A. B.; Shao, T. Temperature-independent, nonoxidative methane conversion in nanosecond repetitively pulsed DBD plasma. *Sustainable Energy Fuels* **2021**, *5*, 787–800.

(46) De Bie, C.; Verheyde, B.; Martens, T.; van Dijk, J.; Paulussen, S.; Bogaerts, A. Fluid Modeling of the Conversion of Methane into Higher Hydrocarbons in an Atmospheric Pressure Dielectric Barrier Discharge. *Plasma Processes and Polymers* **2011**, *8*, 1033–1058.

(47) Sun, J.; Chen, Q. Kinetic roles of vibrational excitation in RF plasma assisted methane pyrolysis. *Journal of Energy Chemistry* **2019**, *39*, 188–197.

(48) Dijk, J. v.; Peerenboom, K.; Jimenez, M.; Mihailova, D.; Mullen, J. v. d. The plasma modelling toolkit Plasimo. *Journal of Physics D: Applied Physics* **2009**, *42*, 194012.

(49) Hagelaar, G. J. M.; Pitchford, L. C. Solving the Boltzmann equation to obtain electron transport coefficients and rate coefficients for fluid models. *Plasma Sources Science and Technology* **2005**, *14*, 722–733.

(50) Neyts, E. C. Plasma-Surface Interactions in Plasma Catalysis. *Plasma Chemistry and Plasma Processing* **2016**, *36*, 185–212.

(51) Bal, K. M.; Huygh, S.; Bogaerts, A.; Neyts, E. C. Effect of plasma-induced surface charging on catalytic processes: application to CO_2 activation. *Plasma Sources Science and Technology* **2018**, *27*, 024001.

(52) Krylov, O. V. Catalytic reactions of partial methane oxidation. *Catalysis Today* **1993**, *18*, 209–302.

(53) Smith, R. R.; Killelea, D. R.; DelSesto, D. F.; Utz, A. L. Preference for Vibrational over Translational Energy in a Gas-Surface Reaction. *Science* **2004**, *304*, 992–995.

(54) Varghese, J. J.; Mushrif, S. H. First-principles investigation of the dissociation and coupling of methane on small copper clusters: Interplay of collision dynamics and geometric and electronic effects. *The Journal of Chemical Physics* **2015**, *142*, 184308.

(55) Jiang, B.; Yang, M.; Xie, D.; Guo, H. Quantum dynamics of polyatomic dissociative chemisorption on transition metal surfaces: mode specificity and bond selectivity. *Chemical Society Reviews* **2016**, *45*, 3621–3640.

(56) Guéret, C.; Daroux, M.; Billaud, F. Methane pyrolysis: thermodynamics. *Chemical Engineering Science* **1997**, *52*, 815–827.

(57) Okolie, C.; Lyu, Y.; Kovarik, L.; Stavitski, E.; Sievers, C. Coupling of Methane to Ethane, Ethylene, and Aromatics over Nickel on Ceria–Zirconia at Low Temperatures. *ChemCatChem* **2018**, *10*, 2700–2708.

(58) Ray, K.; Sengupta, S.; Deo, G. Reforming and cracking of CH_4 over Al_2O_3 supported Ni, Ni-Fe and Ni-Co catalysts. *Fuel Processing Technology* **2017**, *156*, 195–203.

(59) Xu, M.; Lopez-Ruiz, J. A.; Kovarik, L.; Bowden, M. E.; Davidson, S. D.; Weber, R. S.; Wang, I.-W.; Hu, J.; Dagle, R. A. Structure sensitivity and its effect on methane turnover and carbon co-product selectivity in thermocatalytic decomposition of methane over supported Ni catalysts. *Applied Catalysis A: General* **2021**, *611*, 117967.

(60) Maestri, M.; Vlachos, D.; Beretta, A.; Groppi, G.; Tronconi, E. Steam and dry reforming of methane on Rh: Microkinetic analysis and hierarchy of kinetic models. *Journal of Catalysis* **2008**, *259*, 211–222.

(61) Maier, L.; Schädel, B.; Herrera Delgado, K.; Tischer, S.; Deutschmann, O. Steam Reforming of Methane Over Nickel: Development of a Multi-Step Surface Reaction Mechanism. *Topics in Catalysis* **2011**, *54*, 845–858.

(62) Chen, D.; LÃždeng, R.; Svendsen, H.; Holmen, A. Hierarchical Multiscale Modeling of Methane Steam Reforming Reactions. *Industrial & Engineering Chemistry Research* **2011**, *50*, 2600–2612.

(63) Kechagiopoulos, P.; Angeli, S.; Lemonidou, A. Low temperature steam reforming of methane: A combined isotopic and microkinetic study. *Applied Catalysis B: Environmental* **2017**, *205*, 238–253.

(64) Kechagiopoulos, P. N.; Thybaut, J. W.; Marin, G. B. Oxidative Coupling of Methane: A Microkinetic Model Accounting for Intraparticle Surface-Intermediates Concentration Profiles. *Industrial & Engineering Chemistry Research* **2014**, *53*, 1825–1840.

(65) Alexiadis, V.; Thybaut, J.; Kechagiopoulos, P.; Chaar, M.; Van Veen, A.; Muhler, M.; Marin, G. Oxidative coupling of methane: catalytic behaviour assessment via comprehensive microkinetic modelling. *Applied Catalysis B: Environmental* **2014**, *150-151*, 496–505.

(66) Wei, J.; Iglesia, E. Isotopic and kinetic assessment of the mechanism of reactions of CH4 with CO2 or H2O to form synthesis gas and carbon on nickel catalysts. *Journal of Catalysis* **2004**, *224*, 370–383.

(67) Juurlink, L. B. F.; Killelea, D. R.; Utz, A. L. State-resolved probes of methane dissociation dynamics. *Progress In Surface Science* **2009**, *84*, 69–134.

(68) Chen, N.; Huang, Y.; Utz, A. L. State-Resolved Reactivity of Methane ($\nu_2 + \nu_4$) on Ni(111). *The Journal of Physical Chemistry A* **2013**, *117*, 6250–6255.

(69) SriBala, G.; Michiels, D.; Leys, C.; Van Geem, K. M.; Marin, G. B.; Nikiforov, A. Methane reforming to valuable products by an atmospheric pressure direct current discharge. *Journal of Cleaner Production* **2019**, *209*, 655–664.

(70) Xu, C.; Tu, X. Plasma-assisted methane conversion in an atmospheric pressure dielectric barrier discharge reactor. *Journal of Energy Chemistry* **2013**, *22*, 420–425.

(71) Butterworth, T.; Steeg, A. v. d.; Bekerom, D. v. d.; Minea, T.; Righart, T.; Ong, Q.; Rooij, G. v. Plasma induced vibrational excitation of CH_4-a window to its mode selective processing. *Plasma Sources Science and Technology* **2020**, *29*, 095007.

(72) Kasinathan, P.; Park, S.; Choi, W. C.; Hwang, Y. K.; Chang, J.-S.; Park, Y.-K. Plasma-Enhanced Methane Direct Conversion over Particle-Size Adjusted MOx/Al_2O_3 (M = Ti and Mg) Catalysts. *Plasma Chemistry and Plasma Processing* **2014**, *34*, 1317–1330.

TOC Graphic

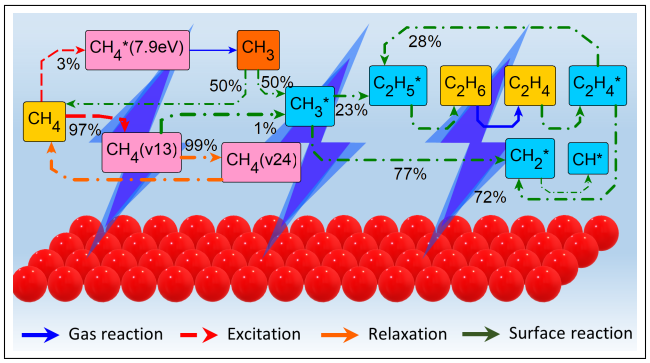
CH4*(7.9eV)
CH3
3%
50%
50%
CH4
97%
CH3*
1%
23%
28%
C2H5*
C2H6
C2H4
C2H4*
CH4(v13)
99%
CH4(v24)
CH2*
CH*
77%
72%
Gas reaction
Excitation
Relaxation
Surface reaction